Published online：2019-02-20 08:35:28
URL：http://kns.cnki.net/kcms/detail/11.5843.P.20190219.1348.002.html

SCIENCE CHINA
Earth Sciences

•PROGRESS•

https://doi.org/10.1007/s11430-019-9330-3

Observational evidences of wave excitation and inverse cascade in a distant Earth foreshock region

Jiansen HE[1*], Die DUAN[1], Xingyu ZHU[1], Limei YAN[2] & Linghua WANG[1]

[1] School of Earth and Space Sciences, Peking University, Beijing 100871, China;
[2] Key Laboratory of Earth and Planetary Physics, Institute of Geology and Geophysics, Chinese Academy of Sciences, Beijing 100029, China

Received January 2, 2019; revised January 14, 2019; accepted January 15, 2019

Abstract The foreshock with nascent plasma turbulence is regarded as a fascinating region to understand basic plasma physical processes, e.g., wave-particle interactions as well as wave-wave couplings. Although there have been plenty of intensive studies on this topic, some key clues about the physical processes still lack observations. A relatively comprehensive case study with some new observations is presented in this work based on the WIND spacecraft observations. In this case, upstream energetic protons were drifting at tens of Alfvén speed with respect to the background plasma protons. When looking at the magnetic wave activities, we find the co-existence of high-frequency (0.1−0.5 Hz) large-amplitude right-hand polarized (RHP) waves and low-frequency (0.02−0.1 Hz) small-amplitude left-hand polarized (LHP) waves in the spacecraft (SC) frame. The observed anti-correlation between magnetic and velocity fluctuations along with the sunward magnetic field direction indicates that the low-frequency LHP waves in the SC frame are in fact the sunward upstream RHP Alfvénic waves in the solar wind frame. This new observation corroborates the applicability of theories about plasma non-resonance instability and inverse cascade to the foreshock region, where the downstream high-frequency RHP parent waves are excited by the upstream energetic protons through non-resonance instability and the low-frequency RHP daughter waves are generated by the parent waves due to nonlinear parametric instability. Furthermore, enhanced downstream energetic proton fluxes are inferred to result from scattering of the upstream protons by the nascent turbulent fluctuations. Therefore, some critical clues about the newborn turbulence in the foreshock are provided in this work.

Keywords Solar wind, Foreshock, Wave-particle interaction, Parametric instability

Citation: He J, Duan D, Zhu X, Yan L, Wang L. 2019. Observational evidences of wave excitation and inverse cascade in a distant Earth foreshock region. Science China Earth Sciences, 62, https://doi.org/10.1007/s11430-019-9330-3

1. Introduction

The foreshock is a region where shock-energized particles are reflected upstream and convected back towards the shock, if it has the fast-mode Mach number larger than the first critical Mach number (Tsurutani and Rodriguez, 1981; Burgess and Scholer, 2013; Wilson, 2016). Since the accelerated ions usually escape from the shock at a speed lower than that of the reflected energetic electrons, the foreshock outer boundary for the ions is closer to the bow shock than the electron foreshock boundary. The extended foreshock region is usually located upstream of the quasi-parallel shock, where the reflected particles can travel upstream along the magnetic field lines reaching to a great distance from the shock (Eastwood et al., 2005). In front of the quasi-perpendicular shock, there are also some activity of dispersive wave, e.g., whistler precursors (Balikhin et al., 1997; Horbury et al., 2001; Bale et al., 2005; Wilson III et al., 2009; Sundkvist et al., 2012). Foreshocks have been found around various shocks in the heliosphere, e.g., the terrestrial bow shock, the bow shocks ahead of other planets and comets, and the shocks ahead of the fast solar wind streams as well as

* Corresponding author (email: jshept@pku.edu.cn)

the fast interplanetary coronal mass ejections (ICMEs) (Vinas et al., 1984; Goldstein et al., 1983; Le et al., 1989; Wilson III et al., 2009). The formation of the global foreshock has been modeled numerically in multi-dimensional hybrid particle-in-cell simulations (Lin and Wang, 2005; Omidi et al., 2009; Karimabadi et al., 2014) and hyrid Vlasov simulations (Palmroth et al., 2015; Kempf et al., 2015). However, almost none of the previous numerical simulations has ever addressed the physical processes occurring in the distant foreshock around the Langrange L1 point with more than 200 Earth radii upstream of the Earth.

Various kinds of wave activities in terms of magnetic field fluctuations are observed in the ion foreshock region (Fairfield, 1969; Le et al., 1992; Narita et al., 2007). The periods of the wave signatures fall in a relatively wide range corresponding to the ultra-low-frequency (ULF) band, which can be less than 1 s or more than 30 s. The magnetic field fluctuations are often observed to have quasi-circular polarization about the local mean magnetic field direction (B_0), being right handed at some times and left handed at other times in the spacecraft (SC) frame. The polarity of the magnetic fluctuation in the solar wind plasma rest frame will be reversed from that in the spacecraft frame, if the wave is propagating upstream in the solar wind frame but thereby carried back downstream and thus measured by the spacecraft from the trailing phase to the leading phase. To identify the wave propagation direction, more information is needed, for example, the correlation between magnetic field and velocity fluctuations or multi-point measurements of the fluctuations with the same phase (Meziane et al., 2007; He et al., 2015; Wang et al., 2015; Yang et al., 2016). Sometimes the magnetic field fluctuations are compressive with the oscillation of magnetic strength being associated with the oscillation of the transverse components. In-phase oscillation of the number density with the magnetic field intensity indicates the nature of compressive fluctuations revealing them to be oblique fast-magnetosonic waves. The incompressible magnetic field fluctuations with left-hand polarization in the plasma rest frame are identified as quasi-parallel Alfvén waves.

It is speculated that the waves are excited by the free energy stored in the upstream energetic protons that are reflected from the bow shock through some instability mechanisms (Gary, 1993; Akimoto et al., 1993). In the ion-ion counter-streams, which are composed of solar wind protons and upstream proton beams, there are four types of ion-ion beam instabilities: (1) LH resonant instability for slow and warm proton beams with $T_\perp / T_\| > 1$; (2) LH non-resonant instability for slow and hot proton beams; (3) RH resonant instability for fast, sparse, and relatively cool proton beams; (4) RH non-resonant instability for fast, dense, and relatively cool proton beams. The waves excited by both RH resonant and LH non-resonant instabilities co-propagate with the upstream proton beams, while the waves generated by RH non-resonant and LH resonant instabilities propagate against the proton beams and towards the bow shock. The excited waves may cause a bump superposed on the background power spectral density (PSD) profile of the magnetic field fluctuations. The bump at the high-frequency subrange of PSD has been previously reported when the interplanetary magnetic field (IMF) is basically in the radial direction, and is conjectured to be a signature of ion-cyclotron resonance instability due to the proton thermal anisotropy in the solar wind, which is presumed to be potentially pristine and unaffected by the foreshock (Gary et al., 2015; Wicks et al., 2016).

The ion-ion counter-streams in the foreshock regions can be characterized as three types of ion velocity distributions (Hoppe and Russell 1982): (1) field-aligned ion beams with narrow spread in the pitch-angle; (2) intermediate ions with relatively larger spread in the pitch-angle of the beams; (3) diffuse ions with a roughly isotropic shell of the energized ions, which are probably pitch-angle scattered from the former two distributions or from ring-beam-like distributions. The reflected ions from the bow shock can cause the apparent slowdown of the disturbed solar wind mean velocity in nonlinear sturctures as observed upstream of the bow shock (Parks et al., 2013). Apart from the types of ion-ion beams, the gyrotropic ring-beam-like distributions as well as the non-gyrotropic gyrophase-bunched ions belong to the type of gyrating ions.

Although various types of waves with different frequencies, polarizations, and compressibilities have been reported case by case at different times/locations, the intrinsic connection between these waves however remains unknown observationally. Not every branch of observed waves is directly excited from a plasma instability. Both theoretical derivaton and numerical simulation illustrate that the waves with lower frequency can be generated by the high-frequency waves through nonlinear wave-wave interactions, which opens the path for an inverse energy cascade (Sagdeev and Galeev, 1969; Araneda et al., 2007). However, the simultaneous observation of both low- and high-frequency waves with the proper polarization as well as the proper propagating direction has still been lacking, though it is required to support the inverse cascade scenario. The inverse cascade may be the underlying physical process for the observed power-law spectra of the magnetic field fluctuations.

If the excited wave of large amplitude exceeds a certain threshold, nonlinear effects are prone to occur during the wave evolution and cause the so-called parametric instabilities (Galeev and Oraevskii, 1963; Wang and Lin, 2003; Araneda et al., 2008; Li et al., 2013; Maneva et al., 2013; Zhao et al., 2015). Thereby the excess wave power beyond the threshold will be cascaded from the primary waves to the daughter waves. There are three types of parametric instabilities for the waves with circular polarization and quasi-parallel propagation. Parametric decay instability generates counter-propagating lower-frequency Alfvén waves and co-propagating slow magnetosonic waves in low plasma beta regime (Derby Jr., 1978; Goldstein, 1978). Modulational instability tends to occur in high plasma beta regime, and produce the daughter waves co-propagating in the same direction as the parent waves (Mio et al., 1976; Nariyuki and Hada, 2006). Beat instability, as the third type of parametric instability, is important for the plasma beta of the order of unity (Hollweg, 1994). However, to our knowledge, simultaneous observation of the primary waves and the daughter waves has yet to be presented. So the scenario of the inverse cascade due to parametric instabilities in the foreshock region needs to be confirmed observationally.

We present a case with some new observational clues about the key physical processes in the foreshock region. Two distinct waves in two adjacent different frequency bands are discovered, and diagnosed to be the parent and daughter waves, respectively. The free energy source for the parent wave excitation is identified to be associated with the fast upstream beam protons that are superposed on the background solar wind protons. The scattering of upstream energetic particles by the waves is also inferred from the relative enhancement in the downstream proton flux as compared with the flux in nearby quiet times. These observations and analysis results will be described in detail in the following sections.

2. New observations of waves in the foreshock region

The data of the case we study are obtained by the WIND spacecraft in about [14:00, 17:00] UT on March 11, 2005. Figure 1 illustrates an overview of this event with some basic observations and related analysis. Figure 1a and 1b show the full day profiles of the magnetic field strength and x-component in the GSE coordinates, which are successively averaged over a time interval of 10 min. As can be seen from Figure 1c−1e, the magnetic field and bulk velocity components in [14:00, 17:00] basically have negative correlations (CC<0), opposite to the ambient correlations. Sunward Alfvén waves are therefore identified by means of the following conditions: $B_{x,\,GSE} > 0$ and CC(d**V**,d**B**) < 0. This is not a pseudo-sunward propagation due to bending of the magnetic field line, since the ambient correlations are not the same as those in the sunward interval. During the sunward interval, suprathermal (strahl) electrons are found to be counter-streaming in the pitch-angle distribution (Figure 1f), a pattern different from the neighboring suprathermal electrons, which travel anti-sunward against the sunward magnetic field line. The second component of the counter-streaming electrons may have come from the other end of closed interplanetary magnetic field (IMF) line rooted on the Sun, or from some place where electrons were reflected. The solar wind electron in the foreshock region has a thermal temperature of about 20 eV, which is lower than the energy level (~165 eV) in Figure 1f. So Figure 1f illustrates the pitch angle distribution of suprathermal electrons. The spectra of the differential flux density for protons and α particles are shown in Figure 1g, which illustrates an evident reduced flux density of α particles in [14:00 20:00] UT. The decrease of α particles would reduce the damping of cascaded waves if they exist (Gao et al., 2013), and hence is in favor of the daughter wave becoming observable. The detailed time variations of dV_y, dB_y, dV_z, and dB_z in [15:30, 16:00] UT are presented in Figure 1h and 1i, which again clearly show that the fluctuations at scales larger than 10 s are sunward propagating Alfvén waves.

To look for the possible source of the upstream suprathermal electrons and Alfvén waves, we investigate the relative geometric relationship between the terrestrial bow shock and the IMF line passing through the WIND spacecraft. The bow shock as predicted from an empirical model in response to the solar wind in [15:30, 16:00] is illustrated as a golden yellow surface in Figure 2. The IMF line (red line in Figure 2), which is represented by the magnetic field vector averaged over the same time interval, is connected with the bow shock. Therefore, it is inferred that the WIND spacecraft was still in the extended foreshock region, though it was more than 200 Re (Earth radii) away from the Earth.

The wave features during [15:30, 16:00] are analyzed in detail in Figure 3. After applying the singular value decomposition method (Santolík et al., 2003) to the magnetic field fluctuations, we find that $\boldsymbol{\theta}(\mathbf{k},\mathbf{b}_0)$ jumps from small to large angles (Figure 3a) and $\boldsymbol{\theta}(d\mathbf{b},\mathbf{b}_0)$ changes from large to small angles (Figure 3b) around the period of 1 s. The scale variation of $\boldsymbol{\theta}(\mathbf{k},\mathbf{b}_0)$ and $\boldsymbol{\theta}(d\mathbf{b},\mathbf{b}_0)$ indicates a transition from quasi-parallel propagating waves with transverse magnetic oscillations at large scales to quasi-perpendicular propagating waves with more longitudinal magnetic oscillations at small scales. At scales larger than 1 s, the sense of the magnetic polarization about the local background magnetic field $\mathbf{B}_0$ in the spacecraft frame shows a distinct contrast at scales below and above 10 s: positive (right hand) polarity in [1, 10] s and negative (left hand) polarity in [10, 50] s (see Figure 3c). Both of these two polarized fluctuations are quasi-circular polarization, since the polarization ellipticity, which is defined as the ratio of the second and first largest singular values, is close to 1 in both scale ranges (Figure 3d). The change of polarity across the scale of 10 s is also confirmed in the wavelet spectra of the normalized reduced fluctuating magnetic helicity ($\boldsymbol{\sigma}_m$) (Figure 3e), the polarity of which describing the rotation about the solar radial direction is basically opposite to that of the magnetic polarization

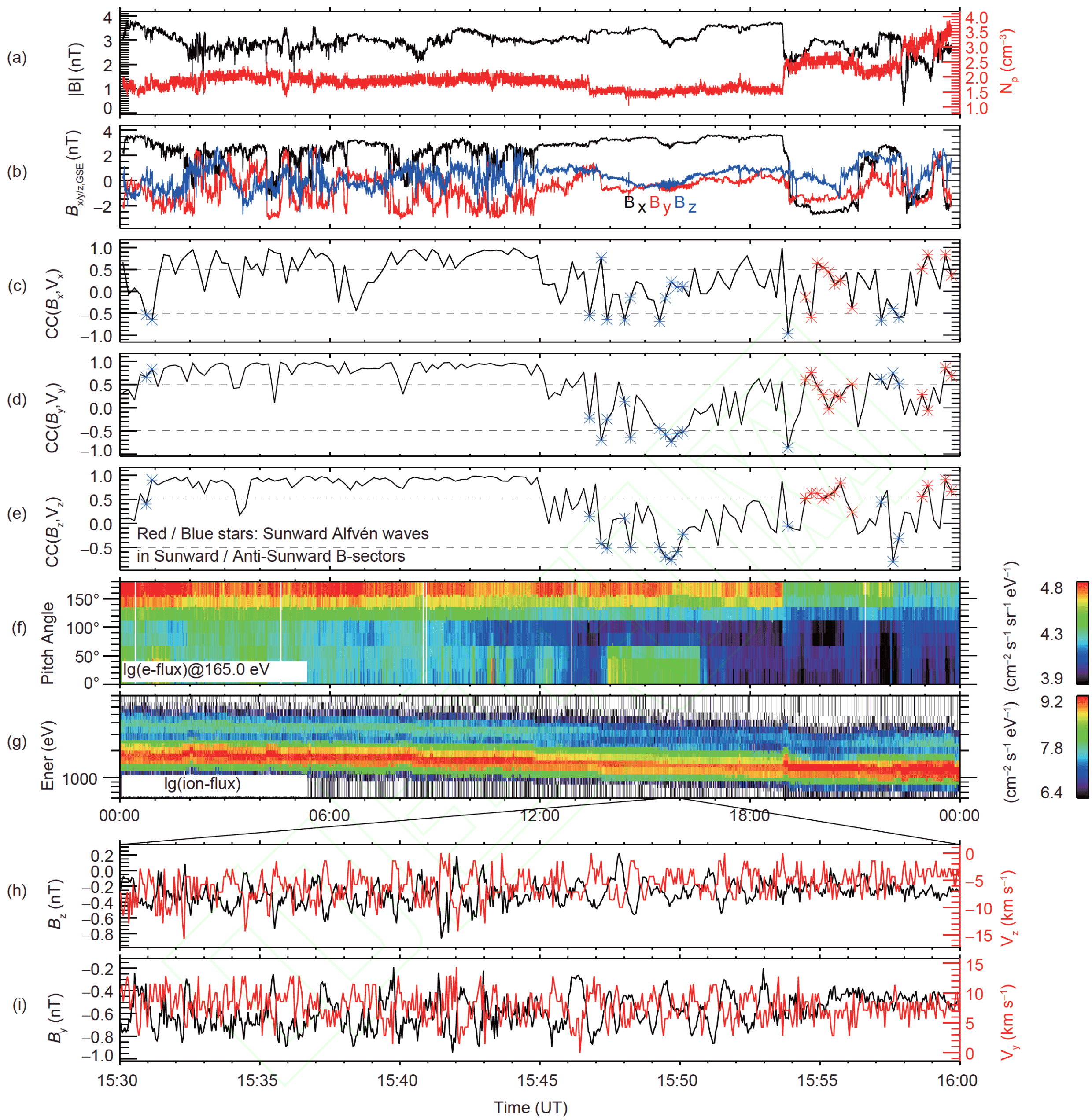

Figure 1 (Color online) (a), (b) Full-day profile of the magnetic field magnitude |B| and the x-component of the magnetic field vector in the GSE coordinates on March 11, 2005. (c)–(e) Correlation coefficients of the variable pairs ((B_x, V_x), (B_y, V_y), and (B_z, V_z)) as calculated every 10 minutes. (f) Pitch-angle distributions of the electron differential flux at the energy channel of 165 eV, showing the existence of counter-streaming electrons during [14:00, 16:00] UT. (g) Energy spectra of the ion differential flux, showing the weak flux of alpha particles during [14:00, 20:00] UT. (h)–(i) Time sequences of B_y, V_y, B_z, and V_z in the interval of [15:30, 16:00] UT, illustrating the good anti-correlations between magnetic field and flow velocity fluctuations.

estimate in Figure 3d at the same scales. The time-varying scale-dependent local mean magnetic field is always pointing sunward, opposite to the radial direction, with all the angles $\theta_{R,B}$ being larger than 150 degrees throughout the whole time intervals and scales.

The left-hand polarization in the SC frame at scales larger than 10 s corresponds to the right-hand polarization of waves in the plasma rest frame, since the waves are propagating sunward along with background magnetic field direction (Figure 1c−1e). Therefore, the waves with scales larger than 10 s may be identified as sunward propagating Alfvén waves with right-hand polarization. It is difficult to identify the propagation direction of the short-wavelength waves with scales smaller than 10 s. There is no clear phase cross-coherence between the magnetic field and velocity fluctuations at small scales, since the velocity measure has relatively weak ratio of signal to noise at higher frequency. Nevertheless, the propagation direction may still be anti-sunward according to the prediction made by the plasma instability theory for the observed upstream proton fast beams and

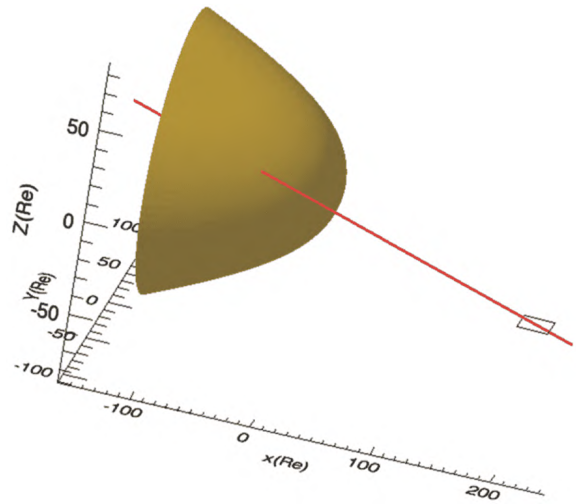

Figure 2 (Color online) The IMF line (red line) passing through the WIND spacecraft (denoted by the rhomboid) intersects with the bow shock, demonstrating that the spacecraft was in the distant foreshock region during [15:30, 16:00] UT.

right-hand magnetic polarization in the SC frame.

The waves at smaller scales (< 10 s) occasionally have the amplitudes larger than their counterpart at larger scales (>10 s), causing a bump in the high-frequency section of the power spectral density (PSD) profile. The top panel of Figure 4 shows one such example of PSD based on the original time sequence between 15:30 and 16:00. The trace power, the power for the local perpendicular fluctuations (PSD($\delta B_\perp$)), and the power for the local parallel fluctuations ($\delta B_\|$) are illustrated by the black, the higher gray, and the lower gray curves in the top panel of Figure 4. It can be seen that the magnetic fluctuations are nearly incompressible, with the parallel power being much smaller than the perpendicular power. The perpendicular fluctuations ($\delta B_\perp$) can be decomposed into two components ($\delta B_{\perp,\ \mathrm{left}}$ and $\delta B_{\perp,\ \mathrm{right}}$) with left and right hand circular polarizations, respectively. The bump of the PSD is mainly contributed by $\delta B_{\perp,\ \mathrm{right}}$ (red curve in the panel), while the lower-frequency band of the PSD is mainly composed of $\delta B_{\perp,\ \mathrm{left}}$ (blue curve). The left and right hand polarizations as decomposed here refer to the polarizations with respect to $\mathbf{B}_{0,\ \mathrm{local}}$ in the spacecraft frame. The hodograms of the B_y and B_z fluctuations (during [15:41, 15:44] with large and small time scales ([15, 30] s and [2, 6] s)) as obtained from the wavelet decomposition, which has been successfully employed to diagnose the kinetic waves in the solar wind turbulence (He et al, 2011), are illustrated in the bottom left and bottom right panels of Figure 4, respectively. The B_x component, which is the main component of the background magnetic field and parallel to the GSE-x direc-

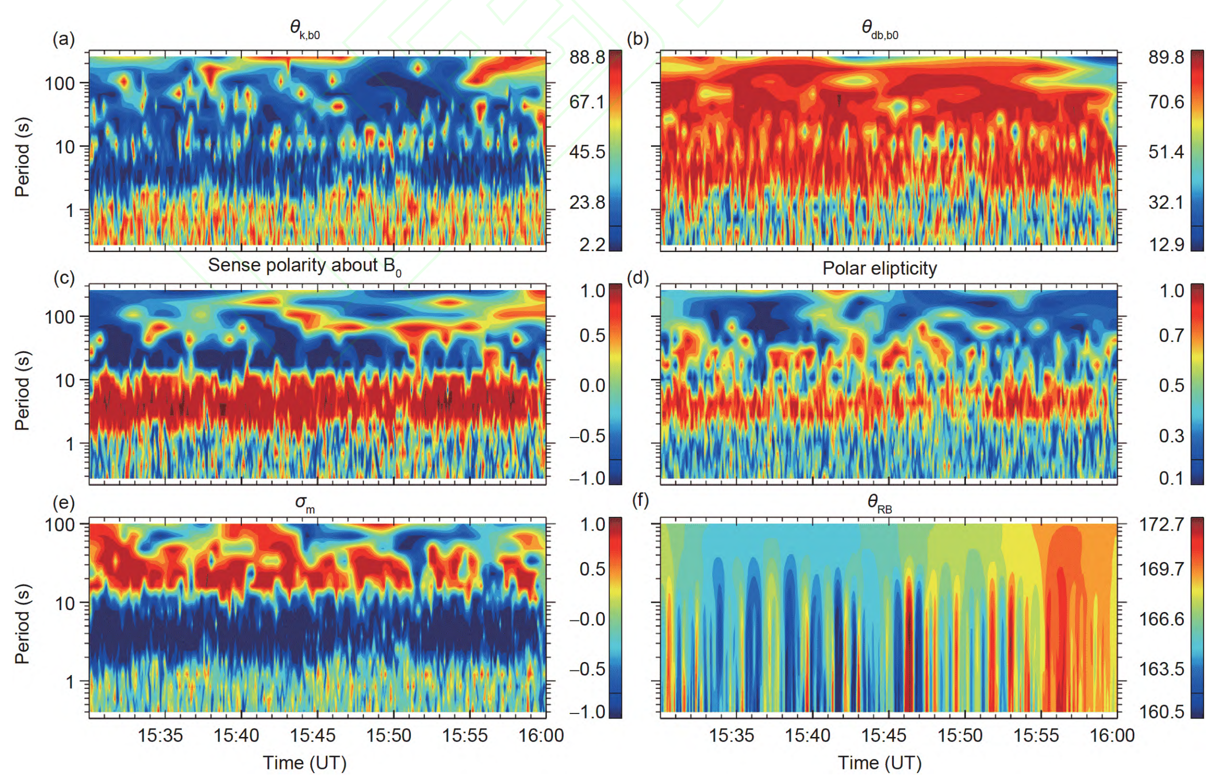

Figure 3 (Color online) (a) Spectra of the angle between the direction with local and scale-dependent minimum magnetic field variance and the direction of local mean magnetic field vector. (b) Spectra of the angle between the direction with local and scale-dependent maximum B-variance and the direction of local $\mathbf{B}_0$. (c) Sense of magnetic polarization about $\mathbf{B}_0$ in the SC frame, with the values of −1 and +1 representing the left-hand and right-hand circular polarization. (d) Ellipticity of the polarization with the values of 0 and 1 denoting the linear and circular polarization. (e) Spectra of the reduced fluctuating magnetic helicity, which shows an evident transition from positive to negative polarity as the time scale decreases from tens of second to less than 10 s. (f) Spectra of the angle between the local $\mathbf{B}_0$ and the solar centric radial direction, illustrating that θ_{RB} is always larger than 150 degrees in the time interval.

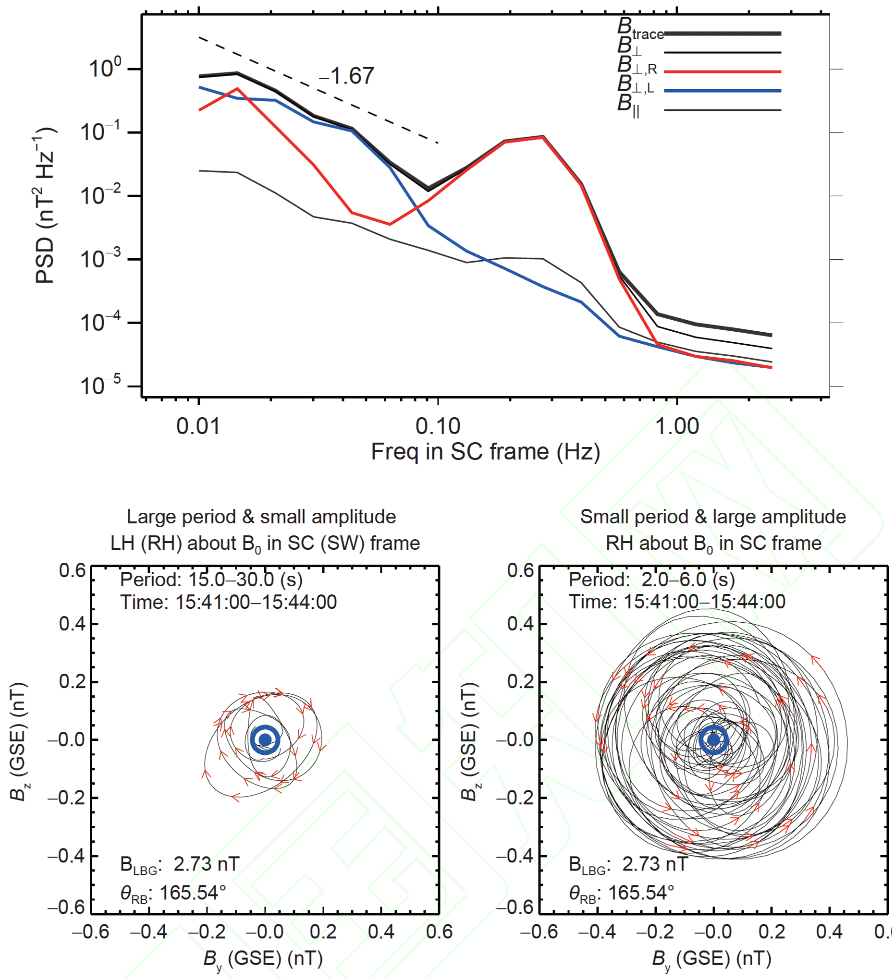

Figure 4 (Color online) Power spectral profiles of different types of magnetic variables: $\delta B_{\mathrm{trace}}$ (black), $\delta B_{\perp}$ (higher gray), $\delta B_{\parallel}$(lower gray), $\delta B_{\perp,\,\mathrm{left}}$ (blue), and $\delta B_{\perp,\,\mathrm{right}}$ (red) in the top panel. These PSDs are calculated from magnetic fluctuations during [15:30, 16:00] UT. Hodograms of the B_y and B_z in the time scale ranges of [15.0, 30.0] s (bottom left) and [2.0, 6.0] s (bottom right). It is shown that the fluctuations of small time scales are right-hand polarization about B_x (the main component of $\mathbf{B}_0$) and large-amplitude, while the large-scale fluctuations are small-amplitude and left-hand polarization.

tion, is pointing out of the plane towards the observer. Therefore, the hodograms in the left and right panels display the left and right hand rotations about B_x in the spacecraft frame. It is also noted that the amplitude of the hodogram in the right panel is about twice of that in the left panel. It is speculated that the enhanced wave power at high frequency may be excited by certain instability and may supply the primary wave energy to be cascaded to the lower frequency. We note that the trace power signal in the high-frequency band is not the residual result due to the non-exact-orthogonal installation of the three sensors of the flux-gate magnetometer, which has been well calibrated recently (Koval and Szabo, 2013).

3. Proton beams as the wave source and their scattering

The enhanced wave power at higher frequency is associated with intense proton beams traveling sunward relative to the major part of solar wind protons. The sunward proton beams emerge on the sunward side of the asymmetric profile of the velocity distribution function when being cut parallel to the magnetic field direction (see for example the red lines with red diamonds in Figure 5a and 5b). The velocity origin in the figure is set approximately at the bulk velocity. The thermal core of the solar wind protons usually gets saturated, when being evaluated by the PESA-High instrument due to the high threshold at low energy, and thereby gets masked by the hashed shadow area in the figure. The red line segment on the left side of the hashed area, which is above the one-count level, is higher than its counterpart on the right side of the hashed area. Therefore, WIND was observing an asymmetric field-aligned velocity distribution. This skewness is contributed from the fast proton beams drifting sunward at high speed (>10V_A) relative to the major part of solar wind protons. These upstream proton beams are believed to originate from the bow shock and penetrate into the foreshock region.

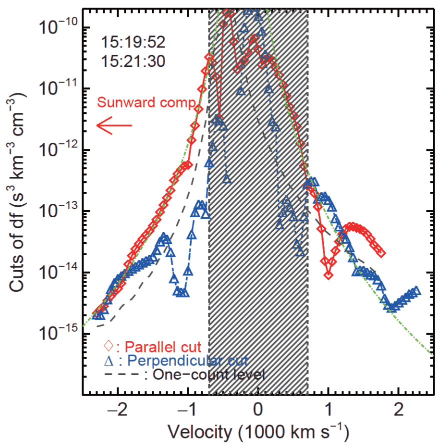

Figure 5 (Color online) Cuts of the proton distribution functions parallel (red lines) and perpendicular (blue lines) to the magnetic fields. The one-count level (gray dash-dot-dot-dot line) is shown for reference. The hashed shadow areas mask the measurements of solar wind proton thermal core, which usually get saturated in the PESA-High instrument. The sunward directions as projected on the magnetic field vector are marked with the red arrows.

Such pattern of the proton velocity distribution may excite the proton-proton beam non-resonance instability, thus producing the RH cyclotron waves propagating anti-parallel to the beam and towards the Earth bow shock. The sunward proton beams appear in the intermediate state between the narrow-angle field-aligned and the fully diffuse contour pattern. In contrast, the cut of the distribution function perpendicular to the magnetic field is basically symmetric about the thermal core (see the blue lines and blue diamonds in Figure 5a and 5b).

The PESA-High instrument is dedicated to measure the ion flux at energies with speed usually higher than 700 km s^{-1}. As compared to PESA-Low, the geometric factor of PESA-High is designed to be significantly higher than that of PESA-Low (1.5×10^{-2} E cm^2 sr eV for the former and 1.6×10^{-4} cm^2 sr eV for the latter) in order to record enough and reliable ion counts of higher energy. Therefore, PESA-Low and PESA-High are complementary to one another in terms of the energy range coverage. On the other hand, fluxes of ions at lower energy as recorded by PESA-High are not reliable due to the possibility of oversaturated sampling under large geometric factor condition, and usually excluded in such analysis. Therefore, the peak of profile is masked by hashed shadow area in Figure 5. To learn the details of the instruments, please refer to (Lin et al., 1995) for the introduction.

A thermal core and adjacent slow beam of the solar wind protons are measured by the PESA-Low instrument and illustrated in Figure 6. There are anti-sunward proton beams drifting faster than the proton cores at about the local Alfvén speed. The reduced field-aligned velocity distributions, which are plotted as the red lines in the lower panels, illustrate another type of asymmetry with enhancement on the anti-sunward wing rather than on the sunward wing. This type of field-aligned asymmetry is the normal state of solar wind protons, which is generally stable and scarcely excites the anti-sunward propagating RH cyclotron waves (Goldstein et al., 2000; Tu et al., 2004; Marsch, 2006; He et al., 2015).

The proton and electron components of the solar wind plasma basically illustrate the conventional patterns of velocity distribution function (VDF). Proton VDFs consist of consist of a core and a field-aligned beam components. Electron VDFs are made up of three types of populations: core, halo, and strahl components. In practice, the proton and electron VDFs can be fitted respectively with functions composed of "core+beam" and "core+halo+strahl", which are listed as followings,

$$\mathrm{VDF}_p = \mathrm{VDF}_{p,core} + \mathrm{VDF}_{p,beam}, \tag{1}$$

$$\mathrm{VDF}_e = \mathrm{VDF}_{e,core} + \mathrm{VDF}_{e,halo} + \mathrm{VDF}_{e,strahl}. \tag{2}$$

The two populations in eq. (1) read as

$$\mathrm{VDF}_{p,core} = N_{p,c}\left(\frac{m_p}{2\pi k_B}\right)^{3/2}\frac{1}{T_{p,c,\perp}T_{p,c,\parallel}^{1/2}}\exp\left(-\frac{m_p}{2k_B}\left(\frac{(V_\parallel - V_{p,c,\parallel,drift})^2}{T_{p,c,\parallel}} + \frac{V_\perp^2}{T_{p,c,\perp}}\right)\right), \tag{3}$$

$$\mathrm{VDF}_{p,beam} = N_{p,b}\left(\frac{m_p}{2\pi k_B}\right)^{3/2}\frac{1}{T_{p,b,\perp}T_{p,b,\parallel}^{1/2}}\exp\left(-\frac{m_p}{2k_B}\left(\frac{(V_\parallel - V_{p,b,\parallel,drift})^2}{T_{p,b,\parallel}} + \frac{V_\perp^2}{T_{p,b,\perp}}\right)\right), \tag{4}$$

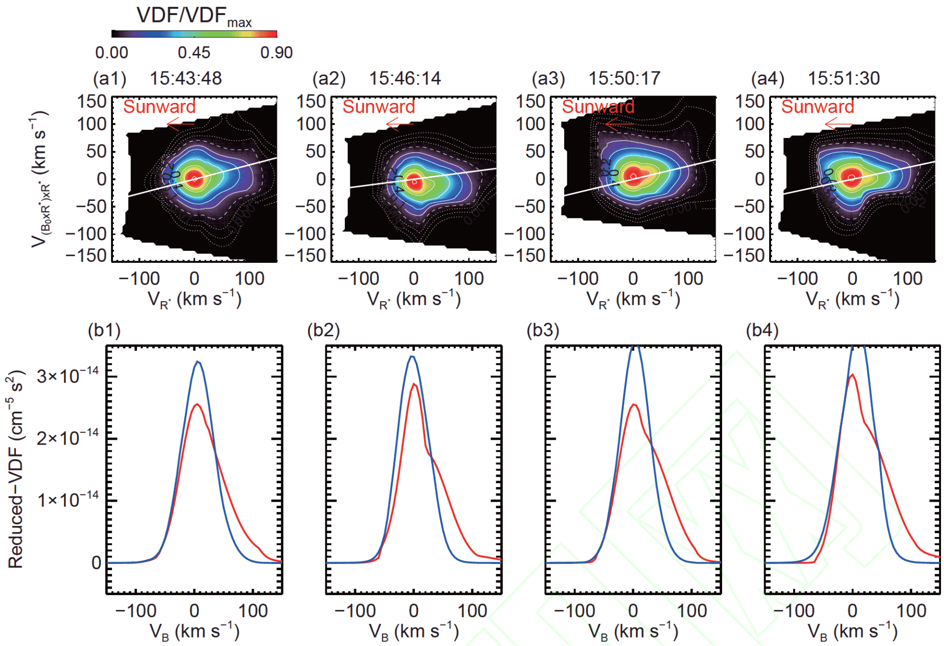

Figure 6 (Color online) (Top panels) 2D cuts of proton velocity distributions as derived from 3DP/PESA-Low measurements at four times with the GSE-x direction (R^* defined as -x in GSE) and the magnetic field direction (B_0) spanning the plane, showing that the field-aligned anti-sunward beams drift relative to the core at around the Alfvén speed. (Bottom panels) Reduced velocity distribution functions (VDFs) at four times as integrated from the VDFs in the plane of (B_0, $R^* \times B_0$) along the direction of $R^* \times B_0$ (blue lines) as well as the direction of B_0 (red lines).

where $N_{p,c}$ and $N_{p,b}$ represent the number densities of proton core and beam components, $T_{p,c,\parallel}$, $T_{p,c,\perp}$, $T_{p,b,\parallel}$, and $T_{p,b,\perp}$ for the parallel and perpendicular temperatures of the core and beam components, $V_{c,\parallel,drift}$ and $V_{b,\parallel,drift}$ for the bulk drift velocities of core and beam components. The constant parameters m_p and k_B represent the proton mass and Boltzmann constant. The parameters to be fitted are as followings: $N_{p,c}$, $N_{p,b}$, $V_{p,c,\parallel,drift}$, $V_{p,b,\parallel,drift}$, $T_{p,c,\parallel}$, $T_{p,c,\perp}$, $T_{p,b,\parallel}$, and $T_{p,b,\perp}$. The formulas for the core, halo, and strahl components of electron VDFs are expressed as

$$\mathrm{VDF}_{e,core} = N_{e,c}\left(\frac{m_e}{2\pi k_B}\right)^{3/2}\frac{1}{T_{e,c,\perp}T_{e,c,\parallel}^{1/2}}\exp\left(-\frac{m_e}{2k_B}\left(\frac{(V_\parallel - V_{e,c,\parallel,drift})^2}{T_{e,c,\parallel}}+\frac{V_\perp^2}{T_{e,c,\perp}}\right)\right), \tag{5}$$

$$\mathrm{VDF}_{e,halo} = A_h\left(1+\frac{m_e}{k_B(2\kappa_h-3)}\right)\left(\frac{V_\perp^2}{T_{e,h,\perp}}+\frac{(V_\parallel - V_{e,h,\parallel,drift})^2}{T_{e,h,\parallel}}\right)^{(-\kappa_h-1)}, \tag{6}$$

$$\mathrm{VDF}_{e,strahl} = A_s\left(1+\frac{m_e}{k_B(2\kappa_s-3)}\right)\left(\frac{V_\perp^2}{T_{e,s,\perp}}+\frac{(V_\parallel - V_{e,s,\parallel,drift})^2}{T_{e,s,\parallel}}\right)^{(-\kappa_s-1)}, \tag{7}$$

where A_h and A_s are expressed as

$$A_h = N_{e,h}\left(\frac{m_e}{\pi k_B(2\kappa_h-3)}\right)^{3/2}\frac{1}{T_{e,h,\perp}T_{e,h,\parallel}^{1/2}}\frac{\Gamma(\kappa_h+1)}{\Gamma(\kappa_h-1/2)}, \tag{8}$$

$$A_s = N_{e,s}\left(\frac{m_e}{\pi k_B(2\kappa_s-3)}\right)^{3/2}\frac{1}{T_{e,s,\perp}T_{e,s,\parallel}^{1/2}}\frac{\Gamma(\kappa_s+1)}{\Gamma(\kappa_s-1/2)}. \tag{9}$$

The parameters to be fitted for electron VDFs include: number densities ($N_{e,c}$, $N_{e,h}$, and $N_{e,s}$), field-aligned drifting velocities ($V_{e,c,\parallel,drift}$, $V_{e,h,\parallel,drfit}$, and $V_{e,s,\parallel,drfit}$), parallel temperatures ($T_{e,c,\parallel}$, $T_{e,h,\parallel}$, and $T_{e,s,\parallel}$), perpendicular temperatures ($T_{e,c,\perp}$, $T_{e,h,\perp}$, and $T_{e,s,\perp}$), κ-exponents (κ_h and κ_s) of κ distributions. The subscripts "*c*", "*h*", and "*s*" are short for "core", "halo", and "strahl" components. As an example, the original and fitted VDFs for protons and electrons of solar wind plasma are illustrated in Figure 7a, 7b, 7c, and 7d. The populations of thermal and suprathermal electrons can be distinguished in Figure 7c, in which the dense core population color-coded in red and yellow is the thermal part and the tenuous periphery population color-coded in green and blue for the suprathermal part.

Bi-directional proton fluxes at the energies between

70 keV and 8 MeV as measured by the WIND/3DP/SST instrument are illustrated in Figure 8. It can be seen that the time profiles of the differential fluxes of the energetic protons travelling parallel to the IMF are almost continuous with few interruptions (see the lines of different colors in Figure 8a), while the differential fluxes of the protons in the anti-parallel case are vacant with data gaps from time to time (see Figure 8b). Since the IMF was pointing mainly towards the Sun, the parallel energetic protons were also travelling upstream towards the Sun. The anti-sunward energetic protons have relatively weak fluxes in most energy channels. The asymmetry between sunward and anti-sunward proton fluxes indicates the predominance of the bow shock over the Sun as an ion source during the considered time interval. It is interesting to find that the anti-sunward proton flux in the energy channel of 130 keV between 14:30 and 16:00 is more evident than at the other times, and comparable to or even higher in level than its counterpart in the sunward direction. This phenomenon seems to result from a scattering of the upstream energetic protons by the nascent turbulence encompassing the excited and cascaded waves.

4. Summary and discussions

We have presented a case with some new observations in the distant foreshock region more than 200 Re away from the Earth when the WIND spacecraft was flying in the halo orbit around the solar-terrestrial L1 point. We find that, even in the distant upstream region, the characteristics of the ion foreshock region remain obvious and clear enough to be measured. The evidences of ion foreshock region lie in as followings: (1) the connection of IMF line between the WIND spacecraft and the flank region of bow shock; (2) the existence of sunward superthermal protons and electrons as reflected from the bow shock and traveling upstream along the IMF line; (3) the associated ULF waves in the period range of [2, 50] s. The good data qualities of both the plasma and magnetic field measurements help us to unambiguously identify the sunward propagation of Alfvénic waves with RH

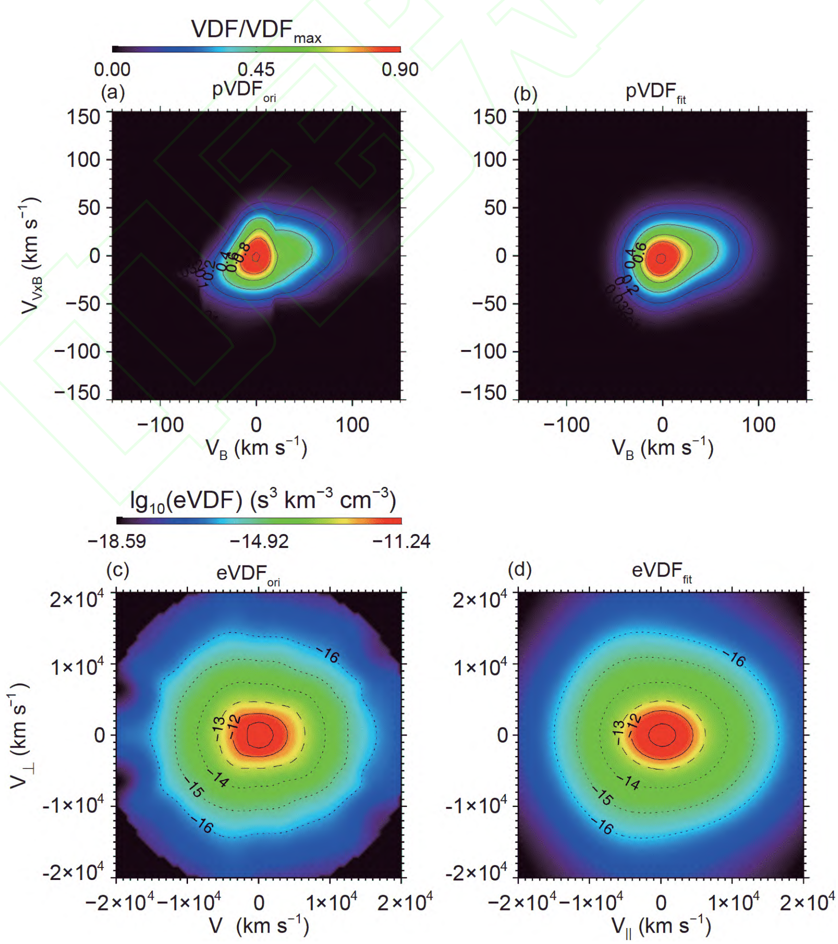

Figure 7 (Color online) Original and fitted velocity distribution functions (VDFs) of solar wind plasmas (protons and electrons). (a) Original solar wind proton VDF illustrating core and beam components as measured from PESA-Low. (b) Fitted solar wind proton VDF as described with eqs. (1), (3), and (4). (c) Original solar wind electron VDF consisting of core, halo, and strahl components as measured from EESA-Low. (d) Fitted solar wind electron VDF according to eqs. (2), (5), (6), and (7).

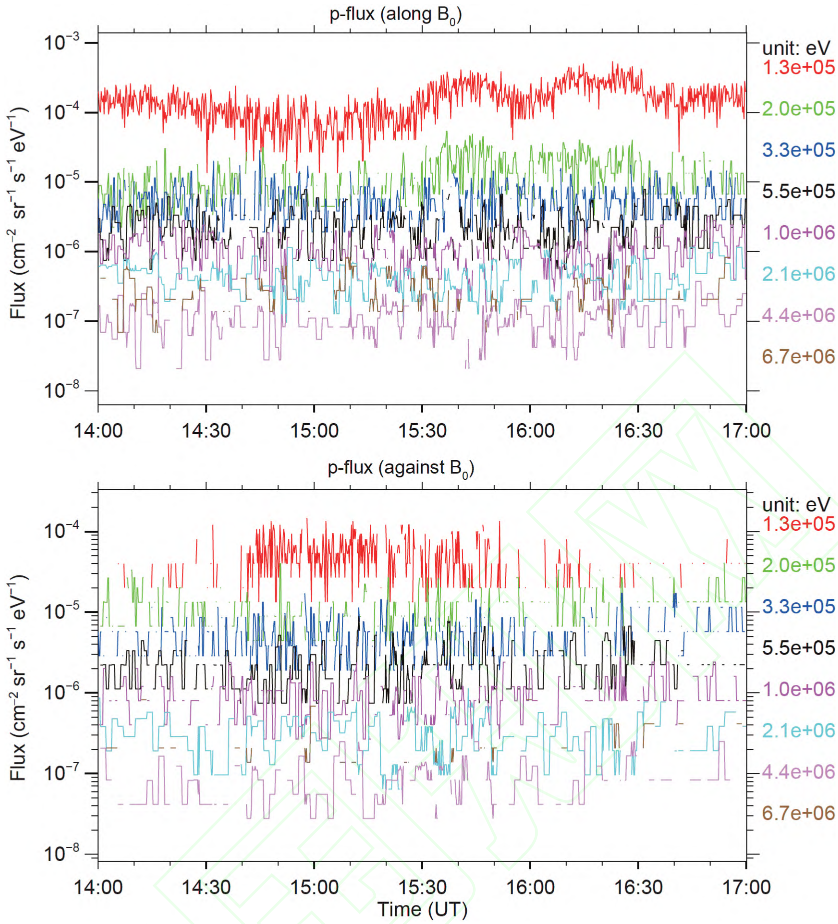

Figure 8 (Color online) Energetic proton differential fluxes of eight energy channels (in different colors) parallel (top) and anti-parallel (bottom) to the local magnetic field B_0 (from 3DP/SST measurements).

polarization in the plasma rest frame at the time scales of [10, 50] s, based on the good anti-correlation between the velocity and magnetic fluctuations in the sunward IMF sector as well as the spectral analysis of the magnetic polarization and reduced helicity. The sunward RH-polarized Alfvénic waves lead to the appearance of LH polarization in the SC frame. Interestingly, at the same time, the magnetic fluctuations at smaller time scales of [2, 10] s illustrate an opposite polarity, RH polarization in the SC frame, one possible nature of which may be the anti-sunward RH cyclotron waves. It seems the first time, as far as we know, that we can report simultaneous observations of two types of waves with opposite magnetic polarizations in the SC frame in two adjacent scale ranges. Moreover, we find that the wave power at the smaller time scales is often stronger than that at the larger time scales, which yields to a bump of the power spectral density in the higher-frequency sub-range.

The observed sunward proton beams, which drift relative to the solar wind proton thermal cores at a speed of the order of 10 V_A, may be responsible for the enhanced high-frequency RH cyclotron waves propagating opposite to the beam direction, whereby the waves are driven through proton-proton beam non-resonance instability (Gary, 1993; Wang and Lin, 2003). When the excited RH cyclotron waves grow to a state of large amplitude, they tend to serve as the parent waves and produce the daughter waves through nonlinear wave coupling, e.g., nonlinear parametric instability as a type of inverse cascade process (Goldstein, 1978; Wang and Lin (2003). The inverse cascade process and result have been observed in previous kinetic simulations, e.g., the hybrid simulation by Wang and Lin (2003). The daughter waves propagate in a direction (sunward) opposite to that for the parent waves (anti-sunward). In association with the wave evolution, the time-evolving particles are also scattered by the waves in the spatial and velocity space. As a scattering result, the upstream energetic particles change from the sunward direction to the anti-sunward direction.

The aforementioned three steps of physical processes involving wave excitation, wave cascading and particle scattering, which are believe to take place in the foreshock region, are sketched in Figure 9. More details about the physics in the foreshock region, for example the evolution of higher-frequency electromagnetic waves and proton-electron dynamics, remain to be unveiled in the future, e.g., by the

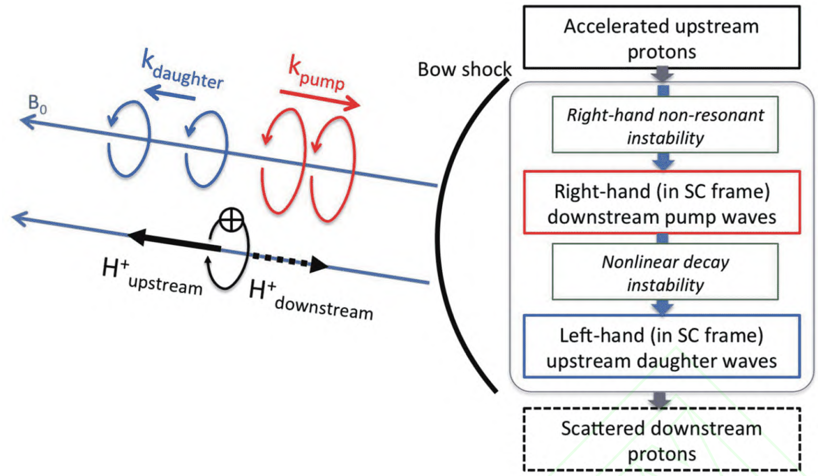

Figure 9 (Color online) Sketch of the three-step physical processes taking place in the foreshock region. The upstream energetic protons as accelerated and reflected from the bow shock are unstable to excite the anti-sunward downstream right-hand cyclotron waves with higher frequency through the ion-ion beam non-resonant instability. The excited waves growing in amplitude are subject to the nonlinear parametric instability and produce the upstream propagating daughter waves with right-hand polarization in the plasma rest frame (left-hand sense in the SC frame). As a feedback, the generated waves scatter the upstream energetic protons back to the downstream direction.

newly operated and proposed missions dedicated to study the coupling between the solar wind and the magnetosphere such as MMS (Magnetospheric Muliti Scale), THOR (Turbulence Heating Observe R), and SMILE (Solar wind Magnetosphere Ionosphere Link Explorer).

Acknowledgements *We thank the 3DP team and MFI team on WIND for sharing data with us. We thank Lynn Wilson III for providing the download of programs, which are used to analyze the PESA-High data. Jiansen He thanks C. H. K. Chen for helpful comments on the calibration of magnetic field data. The group from Peking University is supported by National Natural Science Foundation of China (Grant Nos. 41574168, 41874200, 41674171, 41774183, and 41421003).*

References

Akimoto K, Winske D, Gary S P, Thomsen M F. 1993. Nonlinear evolution of electromagnetic ion beam instabilities. J Geophys Res, 98: 1419–1433
Araneda J A, Marsch E, F.-Viñas A. 2008. Proton core heating and beam formation via parametrically unstable Alfvén-cyclotron waves. Phys Rev Lett, 100: 125003
Araneda J A, Marsch E, Viñas A F. 2007. Collisionless damping of parametrically unstable Alfvén waves. J Geophys Res, 112: A04104
Bale S D, Balikhin M A, Horbury T S, Krasnoselskikh V V, Kucharek H, Möbius E, Walker S N, Balogh A, Burgess D, Lembège B, Lucek E A, Scholer M, Schwartz S J, Thomsen M F. 2005. Quasi-perpendicular shock structure and processes. Space Sci Rev, 118: 161–203
Balikhin M A, de Wit T D, Alleyne H S C K, Woolliscroft L J C, Walker S N, Krasnosel'skikh V, Mier-Jedrzejeowicz W A C, Baumjohann W. 1997. Experimental determination of the dispersion of waves observed upstream of a quasi-perpendicular shock. Geophys Res Lett, 24: 787–790
Burgess D, Scholer M. 2013. Microphysics of Quasi-parallel shocks in collisionless plasmas. Space Sci Rev, 178: 513–533
Derby Jr. N F. 1978. Modulational instability of finite-amplitude, circularly polarized Alfven waves. Astrophys J, 224: 1013–1016
Eastwood J P, Lucek E A, Mazelle C, Meziane K, Narita Y, Pickett J, Treumann R A. 2005. The foreshock. Space Sci Rev, 118: 41–94
Fairfield D H. 1969. Bow shock associated waves observed in the far upstream interplanetary medium. J Geophys Res, 74: 3541–3553
Galeev A A, Oraevskii V N. 1963. The Stability of Alfvén Waves. Soviet Phys Doklady, 7: 988
Gao X, Lu Q, Tao X, Hao Y, Wang S. 2013. Effects of alpha beam on the parametric decay of a parallel propagating circularly polarized Alfven wave: Hybrid simulations. Phys Plasmas, 20: 092106
Gary S P. 1993. Theory of Space Plasma Microinstabilities. Cambridge: Cambridge University Press. 193
Gary S P, Jian L K, Broiles T W, Stevens M L, Podesta J J, Kasper J C. 2015. Ion-driven instabilities in the solar wind: Wind observations of 19 March 2005. J Geophys Res-Space Phys, 121: 30–41
Goldstein B E, Neugebauer M, Zhang L D, Gary S P. 2000. Observed constraint on proton-proton relative velocities in the solar wind. Geophys Res Lett, 27: 53–56
Goldstein M L. 1978. An instability of finite amplitude circularly polarized Alfven waves. Astrophys J, 219: 700–704
Goldstein M L, Smith C W, Matthaeus W H. 1983. Large amplitude MHD waves upstream of the Jovian bow shock. J Geophys Res, 88: 9989–9999
He J, Pei Z, Wang L, Tu C, Marsch E, Zhang L, Salem C. 2015. Sunward propagating Alfvén waves in association with sunward drifting proton beams in the solar wind. Astrophys J, 805: 176
He J, Tu C, Marsch E, Yao S. 2011. Do oblique Alfvén/ion-cyclotron or fast-mode/whistler waves dominate the dissipation of solar wind turbulence near the proton inertial length? Astrophys J, 745: L8
He J, Wang L, Tu C, Marsch E, Zong Q. 2015. Evidence of Landau and cyclotron resonance between protons and kinetic waves in solar wind turbulence. Astrophys J, 800: L31
Hollweg J V. 1994. Beat, modulational, and decay instabilities of a circularly polarized Alfvén wave. J Geophys Res, 99: 23431
Hoppe M M, Russell C T. 1982. Particle acceleration at planetary bow shock waves. Nature, 295: 41–42
Horbury T S, Cargill P J, Lucek E A, Balogh A, Dunlop M W, Oddy T M, Carr C, Brown P, Szabo A, Fornaçon K H. 2001. Cluster magnetic field observations of the bowshock: Orientation, motion and structure. Ann Geophys, 19: 1399–1409
Karimabadi H, Roytershteyn V, Vu H X, Omelchenko Y A, Scudder J, Daughton W, Dimmock A, Nykyri K, Wan M, Sibeck D, Tatineni M, Majumdar A, Loring B, Geveci B. 2014. The link between shocks,

turbulence, and magnetic reconnection in collisionless plasmas. Phys Plasmas, 21: 062308
Kempf Y, Pokhotelov D, Gutynska O, Wilson III L B, Walsh B M, von Alfthan S, Hannuksela O, Sibeck D G, Palmroth M. 2015. Ion distributions in the Earth's foreshock: Hybrid-Vlasov simulation and THEMIS observations. J Geophys Res-Space Phys, 120: 3684–3701
Koval A, Szabo A. 2013. Magnetic field turbulence spectra observed by the wind spacecraft. SOLAR WIND 13: Proceedings of the Thirteenth International Solar Wind Conference. 211–214
Le G, Russell C T, Smith E J. 1989. Discrete wave packets upstream from the earth and comets. J Geophys Res, 94: 3755–3760
Le G, Russell C T, Thomsen M F, Gosling J T. 1992. Observations of a new class of upstream waves with periods near 3 seconds. J Geophys Res, 97: 2917–2925
Li H, Pang Y, Huang S, Zhou M, Deng X, Yuan Z, Wang D, Li H M. 2013. The turbulence evolution in the high β region of the Earth's foreshock. J Geophys Res-Space Phys, 118: 7151–7159
Lin R P, Anderson K A, Ashford S, Carlson C, Curtis D, Ergun R, Larson D, McFadden J, McCarthy M, Parks G K, Rème H, Bosqued J M, Coutelier J, Cotin F, D'Uston C, Wenzel K P, Sanderson T R, Henrion J, Ronnet J C, Paschmann G. 1995. A three-dimensional plasma and energetic particle investigation for the Wind spacecraft. Space Sci Rev, 71: 125–153
Lin Y, Wang X Y. 2005. Three-dimensional global hybrid simulation of dayside dynamics associated with the quasi-parallel bow shock. J Geophys Res, 110: A12216
Maneva Y G, Viñas A F, Ofman L. 2013. Turbulent heating and acceleration of He^{++} ions by spectra of Alfvén-cyclotron waves in the expanding solar wind: 1.5-D hybrid simulations. J Geophys Res-Space Phys, 118: 2842–2853
Marsch E. 2006. Kinetic physics of the solar corona and solar wind. Living Rev Sol Phys, 3: 1
Meziane K, Wilber M, Hamza A M, Mazelle C, Parks G K, Rème H, Lucek E A. 2007. Evidence for a high-energy tail associated with foreshock field-aligned beams. J Geophys Res, 112: A01101
Mio K, Ogino T, Takeda S, Minami K. 1976. Modulational instability and envelope-solitons for nonlinear Alfvén waves propagating along the magnetic field in plasmas. J Phys Soc Jpn, 41: 667–673
Narita Y, Glassmeier K H, Fränz M, Nariyuki Y, Hada T. 2007. Observations of linear and nonlinear processes in the foreshock wave evolution. Nonlin Processes Geophys, 14: 361–371
Nariyuki Y, Hada T. 2006. Remarks on nonlinear relation among phases and frequencies in modulational instabilities of parallel propagating Alfvén waves. Nonlin Processes Geophys, 13: 425–441
Omidi N, Sibeck D G, Blanco-Cano X. 2009. Foreshock compressional boundary. J Geophys Res, 114: A08205
Palmroth M, Archer M, Vainio R, Hietala H, Pfau-Kempf Y, Hoilijoki S, Hannuksela O, Ganse U, Sandroos A, von Alfthan S, Eastwood J P. 2015. ULF foreshock under radial IMF: THEMIS observations and global kinetic simulation Vlasiator results compared. J Geophys Res Space Phys, 120: 8782–8798
Parks G K, Lee E, Lin N, Fu S Y, McCarthy M, Cao J B, Hong J, Liu Y, Shi J K, Goldstein M L, Canu P, Dandouras I, Rème H. 2013. Reinterpretation of slowdown of solar wind mean velocity in nonlinear structures observed upstream of Earth's bow shock. Astrophys J, 771: L39
Sagdeev R Z, Galeev A A. 1969. Nonlinear Plasma Theory. New York: Benjamin
Santolík O, Parrot M, Lefeuvre F. 2003. Singular value decomposition methods for wave propagation analysis. Radio Sci, 38: 1010
Sundkvist D, Krasnoselskikh V, Bale S D, Schwartz S J, Soucek J, Mozer F. 2012. Dispersive nature of high Mach number collisionless plasma shocks: Poynting flux of oblique whistler waves. Phys Rev Lett, 108: 025002
Tsurutani B T, Rodriguez P. 1981. Upstream waves and particles: An overview of ISEE results. J Geophys Res, 86: 4317–4324
Tu C Y, Marsch E, Qin Z R. 2004. Dependence of the proton beam drift velocity on the proton core plasma beta in the solar wind. J Geophys Res, 109: A05101
Vinas A F, Goldstein M L, Acuna M H. 1984. Spectral analysis of magnetohydrodynamic fluctuations near interplanetary shocks. J Geophys Res, 89: 3762–3774
Wang X, Tu C, Wang L, He J, Marsch E. 2015. The upstream-propagating Alfvénic fluctuations with power law spectra in the upstream region of the Earth's bow shock. Geophys Res Lett, 42: 3654–3661
Wang X Y, Lin Y. 2003. Generation of nonlinear Alfvén and magnetosonic waves by beam-plasma interaction. Phys Plasmas, 10: 3528–3538
Wicks R T, Alexander R L, Stevens M, Iii L B W, Moya P S, Viñas A, Jian L K, Roberts D A, O'Modhrain S, Gilbert J A, Zurbuchen T H. 2016. A proton-cyclotron wave storm generated by unstable proton distribution functions in the solar wind. Astrophys J, 819: 6
Wilson L B. 2016. Low Frequency Waves at and Upstream of Collisionless Shocks. In: Andreas Keiling, Dong-Hun Lee, Valery Nakariakov, eds. Low-Frequency Waves in Space Plasmas. Washington DC American Geophysical Union Geophysical Monograph Series, 216: 269–291, doi: 10.1002/9781119055006.ch16
Wilson III L B, Cattell C A, Kellogg P J, Goetz K, Kersten K, Kasper J C, Szabo A, Meziane K. 2009. Low-frequency whistler waves and shocklets observed at quasi-perpendicular interplanetary shocks. J Geophys Res, 114: A10106
Yang L, Lee L C, Chao J K, Hsieh W C, Luo Q Y, Li J P, Shi J K, Wu D J. 2016. Observational evidence for the relationship between Walén slope and amplitude ratio of inward to outward Alfvén waves in the solar wind. Astrophys J, 817: 178
Zhao J S, Voitenko Y, De Keyser J, Wu D J. 2015. Scalar and vector nonlinear decays of low-frequency Alfvén waves. Astrophys J, 799: 222

(Responsible editor: Xueshang FENG)